Kukkola, Jarno; Hinkkanen, Marko

State observer for grid-voltage sensorless control of a converter under unbalanced conditions

Published in:
IEEE Transactions on Industry Applications

DOI:
10.1109/TIA.2017.2749305

Published: 01/01/2018

Document Version
Peer-reviewed accepted author manuscript, also known as Final accepted manuscript or Post-print

Please cite the original version:
Kukkola, J., & Hinkkanen, M. (2018). State observer for grid-voltage sensorless control of a converter under unbalanced conditions. *IEEE Transactions on Industry Applications*, *54*(1), 286-297. https://doi.org/10.1109/TIA.2017.2749305

State Observer for Grid-Voltage Sensorless Control of a Converter Under Unbalanced Conditions

Jarno Kukkola and Marko Hinkkanen, *Senior Member, IEEE*

***Abstract*—This paper deals with grid-voltage sensorless synchronization and control under unbalanced grid conditions. A three-phase grid-connected converter equipped with an LCL filter is considered, and no other signals than the converter currents and the DC-link voltage are measured for control. An augmented adaptive state observer is proposed for estimation of the positive- and negative-sequence components of the grid voltage. Dynamic performance limitations of the proposed method and effects of parameter errors are analysed. The proposed observer is tested as a part of a sensorless control system. Experimental results show that the proposed method works well even in highly unbalanced grid conditions.**

***Index Terms*—Active front-end rectifier, grid-voltage sag, LCL filter, line-voltage sensorless, small-signal linearization.**

I. Introduction

Grid-voltage sensorless control has been an interesting research topic during the last decades [1]–[20]. Replacing AC-voltage sensors with estimation is a relevant option, e.g., in pulse-width-modulated rectifiers [1]–[6], since reducing the number of the sensors can improve the reliability against electrical noise and reduce costs of the system. Furthermore, the grid-voltage sensorless operation has been proposed for distributed generation [8], [9]. Sensorless control, in parallel with the conventional operation, could increase reliability of a converter in renewable energy production, since a failure in measurement sensors, wires, or interfaces does not necessarily mean the end of production. In addition, a grid-voltage estimator might be useful in the islanding detection [11].

In the distributed generation, dynamic grid support, such as fault ride-through, is often required in high- and medium-voltage grids, but might be required in low-voltage grids as well in the future [21]. Furthermore, the converters may operate, at least temporarily, in unbalanced grid conditions [22], [23]. With careful design, unbalanced conditions can be also handled in grid-voltage sensorless control [4], [6], [9], [12]–[15], [19].

An LCL filter between the converter and the grid is an attractive option for filtering out the switching harmonics, because of its higher attenuation per volume or cost in comparison with the conventional L filter. Grid-voltage sensorless methods for converters equipped with the LCL filter have been proposed in [5], [8]–[10], [13]–[20]. The sensorless operation can be based on instantaneous power theory [10], virtual flux models, [5], [14]–[16], and model-based observers [8], [13], [17]–[20]. However, only a few of these methods take unbalanced grid conditions into account [9], [13]–[15], [19].

For the unbalanced grid conditions, a direct power control method has been developed in [14], but additional capacitor current measurements are needed for the active damping of the LCL-filter resonance. Additional capacitor current measurements have been used in [13] as well, where the grid-voltage estimation method is based on an adaptive algorithm [8]. In [9], an adaptive neural-network estimator has been proposed for disturbance and grid-voltage estimation. However, expertise in neural networks is needed in order to implement this type of estimator and to guarantee its stability. In [19], an adaptive model-based state observer has been used in grid-voltage sensorless control, but only the positive-sequence component of the grid voltage is estimated. In [15], grid-voltage sensorless operation is based on a virtual-flux model using a second-order generalized integrator as a fundamental building block. The method in [15] is an extension for the estimator proposed in [12].

This work [24] deals with grid-voltage sensorless synchronization and control of a grid-connected converter under unbalanced grid conditions. A converter equipped with an LCL filter is considered, and the only measured quantities for control are the converter currents and DC-link voltage. Main contributions of this work are: 1) an augmented adaptive state observer is proposed for estimation of the positive- and negative-sequence components of the grid voltage; 2) tuning expressions for the observer are derived based on a small-signal linearized model and direct pole placement; 3) dynamic behavior of the observer is analyzed using the linearized model; 4) effects of parameter errors on steady-state estimation errors are examined; and 5) the proposed observer is experimentally tested as a part of a grid-voltage sensorless control system in unbalanced grid conditions.

II. System Model

The equivalent circuit model of the LCL filter between the converter and the grid is shown in Fig. 1(a). The converter voltage is $\boldsymbol{u}_\mathrm{c}^\mathrm{s}$ and the converter current is $\boldsymbol{i}_\mathrm{c}^\mathrm{s}$, where the superscript s indicates stationary coordinates. The voltage across the filter capacitor is $\boldsymbol{u}_\mathrm{f}^\mathrm{s}$, the grid voltage is $\boldsymbol{u}_\mathrm{g}^\mathrm{s}$, and the grid current is $\boldsymbol{i}_\mathrm{g}^\mathrm{s}$. Complex-valued, matrix, and vector quantities are marked with boldface symbols.

In the case of unbalanced grid conditions (e.g. during a single- or two-phase fault), the grid-voltage vector

$$\boldsymbol{u}_\mathrm{g}^\mathrm{s}(t) = \boldsymbol{u}_\mathrm{g+}^\mathrm{s}(t) + \boldsymbol{u}_\mathrm{g-}^\mathrm{s}(t) = \mathrm{e}^{\mathrm{j}\vartheta_\mathrm{g+}(t)}u_\mathrm{g+} + \mathrm{e}^{\mathrm{j}\vartheta_\mathrm{g-}(t)}u_\mathrm{g-} \quad (1)$$

This work was supported in part by ABB Oy, in part by Finnish Foundation for Technology Promotion, in part by Emil Aaltonen Foundation, and in part by Walter Ahlström Foundation.

J. Kukkola is with ABB Drives, Helsinki, Finland (e-mail: jarno.kukkola@fi.abb.com)

M. Hinkkanen is with Aalto University, Department of Electrical Engineering and Automation, Espoo, Finland (e-mail: marko.hinkkanen@aalto.fi).

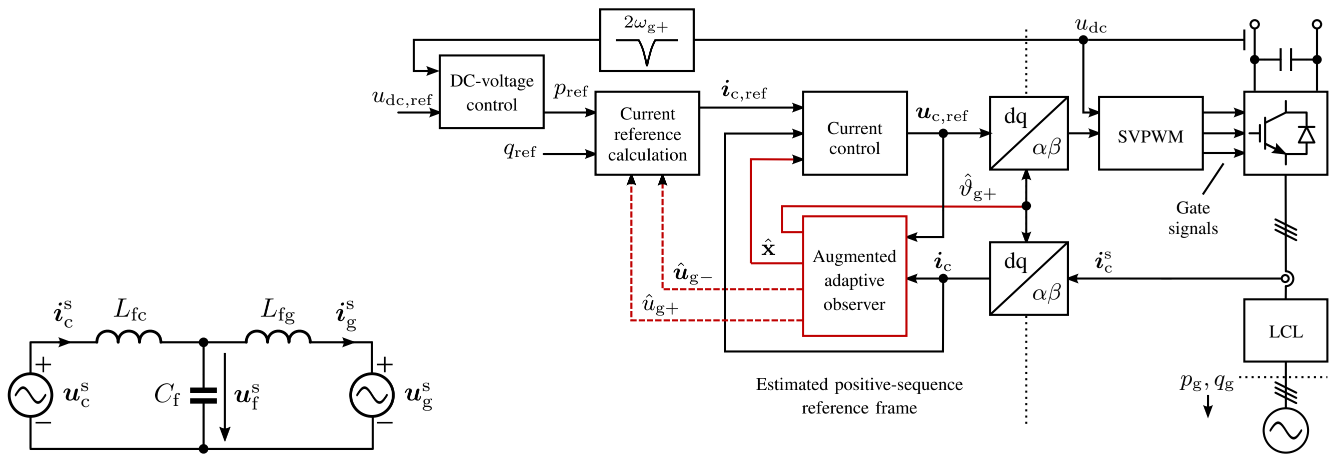

(a) (b)

Fig. 1. (a) Space-vector circuit model of the LCL filter between the converter and the grid. (b) Grid-voltage sensorless control system.

has the positive-sequence and negative-sequence components, $\boldsymbol{u}^s_{g+}$ and $\boldsymbol{u}^s_{g-}$, respectively. The positive-sequence magnitude is u_{g+} and the angle is

$$\vartheta_{g+}(t) = \int \omega_{g+} \mathrm{d}t \tag{2}$$

where ω_{g+} is the fundamental angular frequency of the grid voltage. For the negative-sequence component, u_{g-} is the magnitude, $\vartheta_{g-} = -\vartheta_{g+} + \phi_{g-}$ is the angle, and ϕ_{g-} is the phase shift.

A state-space model is formed from the equivalent circuit of the LCL filter [Fig. 1(a)]. The state vector is selected as $\mathbf{x}^s = [\boldsymbol{i}^s_c, \boldsymbol{u}^s_f, \boldsymbol{i}^s_g]^T$. Moreover, the model is written in positive-sequence coordinates (*marked with the superscript* p). In these coordinates, the state vector is $\mathbf{x}^p = e^{-j\vartheta_{g+}}\mathbf{x}^s$, and other vector quantities are transformed in similar fashion. When the modeling principles presented in [25] are followed, the dynamics of the converter current $\boldsymbol{i}^p_c$ become

$$\begin{aligned}\mathbf{x}^p(k+1) &= \boldsymbol{\Phi}\mathbf{x}^p(k) + \boldsymbol{\Gamma}_c\boldsymbol{u}^p_c(k) + \boldsymbol{\Gamma}_{g+}u_{g+}(k) \\ &\quad + \boldsymbol{\Gamma}_{g-}\boldsymbol{u}^p_{g-}(k) \\ \boldsymbol{i}^p_c(k) &= \mathbf{C}_c\mathbf{x}^p(k)\end{aligned} \tag{3}$$

where $\mathbf{C}_c = [1, 0, 0]$ is the output vector, $\boldsymbol{\Phi}$ is the state-transition matrix, $\boldsymbol{\Gamma}_c$ is the input vector for the converter voltage, and $\boldsymbol{\Gamma}_{g+}$ and $\boldsymbol{\Gamma}_{g-}$ are the input vectors for the positive- and negative-sequence components of the grid voltage, respectively. Symbolic expressions for calculating the model matrices are given in Appendix A.

In the discrete-time domain, the positive-sequence angle (2) is

$$\vartheta_{g+}(k+1) = \vartheta_{g+}(k) + T_s\omega_{g+} \tag{4}$$

where T_s is the sampling time. Furthermore, in positive-sequence coordinates, the rotating negative-sequence component satisfies the difference equation

$$\boldsymbol{u}^p_{g-}(k+1) = e^{-2j\omega_{g+}T_s}\boldsymbol{u}^p_{g-}(k) \tag{5}$$

For the purposes of disturbance estimation, the system model (3) is augmented with the negative sequence (5) as

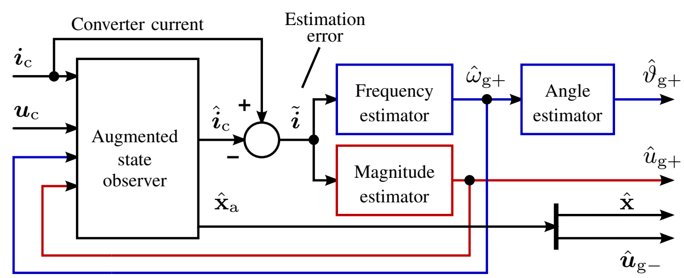

Fig. 2. Augmented adaptive observer.

a disturbance state. The augmented state vector is $\mathbf{x}^p_a = [\boldsymbol{i}^p_c, \boldsymbol{u}^p_f, \boldsymbol{i}^p_g, \boldsymbol{u}^p_{g-}]^T$, and the augmented system model is

$$\begin{aligned}\mathbf{x}^p_a(k+1) &= \underbrace{\begin{bmatrix}\boldsymbol{\Phi} & \boldsymbol{\Gamma}_{g-} \\ \mathbf{0} & e^{-2j\omega_{g+}T_s}\end{bmatrix}}_{\boldsymbol{\Phi}_a}\mathbf{x}^p_a(k) + \underbrace{\begin{bmatrix}\boldsymbol{\Gamma}_c \\ 0\end{bmatrix}}_{\boldsymbol{\Gamma}_{ca}}\boldsymbol{u}^p_c(k) \\ &\quad + \underbrace{\begin{bmatrix}\boldsymbol{\Gamma}_{g+} \\ 0\end{bmatrix}}_{\boldsymbol{\Gamma}_{ga}}u_{g+}(k) \\ \boldsymbol{i}^p_c(k) &= \underbrace{\begin{bmatrix}\mathbf{C}_c & 0\end{bmatrix}}_{\mathbf{C}_a}\mathbf{x}^p_a(k)\end{aligned} \tag{6}$$

III. Augmented Adaptive Observer

The proposed augmented adaptive observer is a part of a sensorless control system shown in Fig. 1(b). The structure of the proposed observer is shown in Fig. 2. While the augmented state vector $\mathbf{x}^p_a$ is estimated based on the model (6), the angular frequency $\hat{\omega}_{g+}$, positive-sequence angle $\hat{\vartheta}_{g+}$, and positive-sequence magnitude $\hat{u}_{g+}$ are estimated using adaptation mechanisms that are explained later.

The observer operates in estimated positive-sequence coordinates (*marked without any superscripts*). According to (4), the positive-sequence angle estimator is

$$\hat{\vartheta}_{g+}(k+1) = \hat{\vartheta}_{g+}(k) + T_s\hat{\omega}_{g+} \tag{7}$$

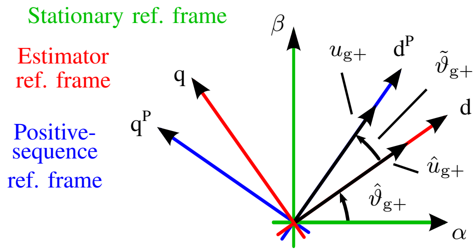

Fig. 3. Relations between the different reference frames.

The estimated positive-sequence coordinate system is generally different from the actual positive-sequence coordinate system due to the possible estimation error $\tilde{\vartheta}_{g+} = \vartheta_{g+} - \hat{\vartheta}_{g+}$, as illustrated in Fig 3.

In estimated coordinates, the augmented state vector is $\mathbf{x}_a = [\mathbf{x}^T, \boldsymbol{u}_{g-}]^T$, and according to (6), the augmented state observer is

$$\hat{\mathbf{x}}_a(k+1) = \hat{\mathbf{\Phi}}_a \hat{\mathbf{x}}_a(k) + \hat{\mathbf{\Gamma}}_{ca}\boldsymbol{u}_c(k) + \hat{\mathbf{\Gamma}}_{ga}\hat{u}_{g+}(k) + \mathbf{K}_o[\boldsymbol{i}_c(k) - \hat{\boldsymbol{i}}_c(k)] \tag{8}$$

where $\hat{\mathbf{\Phi}}_a$, $\hat{\mathbf{\Gamma}}_{ca}$, and $\hat{\mathbf{\Gamma}}_{ga}$ are the adaptive model matrices that are obtained by replacing the actual angular frequency ω_{g+} with the estimated angular frequency $\hat{\omega}_{g+}$ in (6). Furthermore, $\mathbf{K}_o$ is the observer gain vector and $\hat{\boldsymbol{i}}_c(k) = \mathbf{C}_a\hat{\mathbf{x}}_a(k)$.

A. Estimation-Error Dynamics

The estimation-error dynamics, derived in the following, play a key role in the tuning of the proposed observer. First, from (4) and (7), the dynamics of the angle estimation error become

$$\tilde{\vartheta}_{g+}(k+1) = \tilde{\vartheta}_{g+}(k) + T_s\tilde{\omega}_{g+}, \tag{9}$$

where $\tilde{\omega}_{g+} = \omega_{g+} - \hat{\omega}_{g+}$ is the estimation error of the angular frequency. The system model (6) and the observer (8) are in different coordinates. For calculation of the state estimation error, the system model is transformed into estimated positive-sequence coordinates, where the observer operates (cf. Fig. 3). The transformation of the state vector is

$$\mathbf{x}_a^p(k) = e^{-j\tilde{\vartheta}_{g+}(k)}\mathbf{x}_a(k) \tag{10}$$

and $\boldsymbol{u}_c^p$ and $\boldsymbol{i}_c^p$ are transformed similarly. The state vector at $k+1$ is transformed as $\mathbf{x}_a^p(k+1) = e^{-j\tilde{\vartheta}_{g+}(k+1)}\mathbf{x}_a(k+1)$. Together with (9), the transformed system model becomes

$$\begin{aligned}\mathbf{x}_a(k+1) &= e^{jT_s\tilde{\omega}_{g+}(k)}\mathbf{\Phi}_a\mathbf{x}_a(k) + e^{jT_s\tilde{\omega}_{g+}(k)}\mathbf{\Gamma}_{ca}\boldsymbol{u}_c(k) \\ &\quad + e^{j\tilde{\vartheta}_{g+}(k+1)}\mathbf{\Gamma}_{ga}u_{g+}(k) \\ \boldsymbol{i}_c(k) &= \mathbf{C}_a\mathbf{x}_a(k)\end{aligned} \tag{11}$$

The estimation error of the augmented state vector is $\tilde{\mathbf{x}}_a = \mathbf{x}_a - \hat{\mathbf{x}}_a$. From (8), (9), and (11), the estimation-error dynamics become

$$\begin{aligned}\tilde{\mathbf{x}}_a(k+1) &= (\hat{\mathbf{\Phi}}_a - \mathbf{K}_o\mathbf{C}_a)\tilde{\mathbf{x}}_a(k) \\ &\quad + \left(e^{jT_s\tilde{\omega}_{g+}(k)}\mathbf{\Phi}_a - \hat{\mathbf{\Phi}}_a\right)\mathbf{x}_a(k) \\ &\quad + \left(e^{jT_s\tilde{\omega}_{g+}(k)}\mathbf{\Gamma}_{ca} - \hat{\mathbf{\Gamma}}_{ca}\right)\boldsymbol{u}_c(k) + \hat{\mathbf{\Gamma}}_{ga}\tilde{u}_{g+}(k) \\ &\quad + \left(e^{j[\tilde{\vartheta}_{g+}(k) + T_s\tilde{\omega}_{g+}(k)]}\mathbf{\Gamma}_{ga} - \hat{\mathbf{\Gamma}}_{ga}\right)u_{g+}(k)\end{aligned} \tag{12}$$

where $\tilde{u}_{g+} = u_{g+} - \hat{u}_{g+}$ is the estimation error of the positive-sequence magnitude. The estimation-error dynamics (12) are complicated and nonlinear with respect to the estimation errors $\tilde{\vartheta}_{g+}$ and $\tilde{\omega}_{g+}$. Nonlinear elements are also hidden in the matrices marked with a hat, which are indirectly functions of $\tilde{\omega}_{g+}$, since they are functions of $\hat{\omega}_{g+}$. For example, $\hat{\mathbf{\Phi}}_a(\hat{\omega}_{g+}) = \hat{\mathbf{\Phi}}_a(\omega_{g+} - \tilde{\omega}_{g+})$.

B. Small-Signal Linearization

The nonlinear estimation-error dynamics (12) are linearized at an equilibrium point (generally a trajectory). The equilibrium-point quantities are marked with the subscript 0. If the accurate equivalent circuit parameters (L_{fc}, C_f, L_{fg}) are assumed in the observer, the system (12) has an equilibrium point $\{\tilde{\mathbf{x}}_{a0} = \mathbf{0}, \tilde{u}_{g+,0} = 0, \tilde{\omega}_{g+,0} = 0, \tilde{\vartheta}_{g+,0} = 0\}$, where the steady-state estimation errors are zero. Close to the equilibrium point, the dynamics are described by a linear state equation

$$\begin{aligned}\tilde{\mathbf{x}}_a(k+1) &= (\mathbf{\Phi}_a - \mathbf{K}_o\mathbf{C}_a)\tilde{\mathbf{x}}_a(k) + \mathbf{\Gamma}_{ga}\tilde{u}_{g+}(k) \\ &\quad + j\mathbf{\Gamma}_{ga}u_{g+,0}\tilde{\vartheta}_{g+}(k) + \mathbf{\Gamma}_\omega\tilde{\omega}_{g+}(k)\end{aligned} \tag{13}$$

where $\mathbf{\Gamma}_\omega$ is the input vector for the angular-frequency estimation error. These linearized dynamics are derived in Appendix B.

In order to simplify the tuning of the adaptive observer, the linearized dynamics can be further simplified by approximating $\mathbf{\Gamma}_\omega \approx 0$. The approximation is reasonable, since the impact of the input $\tilde{\omega}_{g+}(k)$ on $\tilde{\mathbf{x}}_a(k+1)$ is small[1] in comparison with the other inputs ($\tilde{u}_{g+}$ and $\tilde{\vartheta}_{g+}$). The simplified dynamics are

$$\begin{aligned}\tilde{\mathbf{x}}_a(k+1) &\approx (\mathbf{\Phi}_a - \mathbf{K}_o\mathbf{C}_a)\tilde{\mathbf{x}}_a(k) + \mathbf{\Gamma}_{ga}\tilde{u}_{g+}(k) \\ &\quad + j\mathbf{\Gamma}_{ga}u_{g+,0}\tilde{\vartheta}_{g+}(k)\end{aligned} \tag{14}$$

The converter-current estimation error $\tilde{\boldsymbol{i}}_c = \mathbf{C}_a\tilde{\mathbf{x}}_a$ is the input for the positive-sequence frequency and magnitude estimators, cf. Fig. 2. In order to tune the estimators, the impact of $\tilde{u}_{g+}$ and $\tilde{\vartheta}_{g+}$ on $\tilde{\boldsymbol{i}}_c$ is studied. From (14), the pulse-transfer function from $\tilde{u}_{g+}$ to $\tilde{\boldsymbol{i}}_c$ becomes

$$\boldsymbol{G}_{iu}(z) = \frac{\tilde{\boldsymbol{i}}_c(z)}{\tilde{u}_{g+}(z)} = \mathbf{C}_a(z\mathbf{I} - \mathbf{\Phi}_a + \mathbf{K}_o\mathbf{C}_a)^{-1}\mathbf{\Gamma}_{g+} = \frac{\boldsymbol{b}(z)}{\boldsymbol{a}(z)} \tag{15}$$

where

$$\boldsymbol{a}(z) = \det(z\mathbf{I} - \mathbf{\Phi}_a + \mathbf{K}_o\mathbf{C}_a) \tag{16}$$

and $\boldsymbol{b}(z)$ is the numerator of the transfer function. Similarly, the pulse-transfer function from $\tilde{\vartheta}_{g+}$ to $\tilde{\boldsymbol{i}}_c$ becomes

$$\boldsymbol{G}_{i\vartheta}(z) = \frac{\tilde{\boldsymbol{i}}_c(z)}{\tilde{\vartheta}_{g+}(z)} = \frac{ju_{g+,0}\cdot\boldsymbol{b}(z)}{\boldsymbol{a}(z)} \tag{17}$$

[1]The impact of the inputs at k on $\tilde{\mathbf{x}}_a(k+1)$ can be evaluated by calculating the gains $\|\mathbf{\Gamma}_\omega\|$ and $\|\mathbf{\Gamma}_{ga}\|$. Starting from the equilibrium $\tilde{\mathbf{x}}_a(k) = \mathbf{0}$, the change $\|\tilde{\mathbf{x}}_a(k+1)\|$ in the states caused by the change equal to unity in $\tilde{\omega}_{g+}(k)$ is $\|\mathbf{\Gamma}_\omega\|$. For example, with the parameters of Table I and symmetrical grid-voltage conditions, the gain $\|\mathbf{\Gamma}_\omega\| = 0.01$ p.u. whereas the gain $\|\mathbf{\Gamma}_{ga}\| = \|j\mathbf{\Gamma}_{ga}u_{g+,0}\| = 0.56$ p.u.

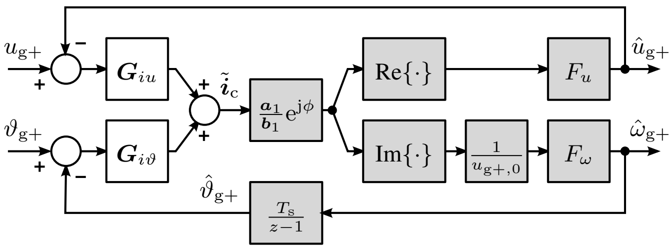

Fig. 4. Linearized estimation-error dynamics for the tuning of the adaptation loops. The approximation $\mathbf{\Gamma}_\omega = 0$ is considered as in (14). The grey blocks represent the estimation algorithms for $\hat{u}_{g+}$, $\hat{\omega}_{g+}$, and $\hat{\vartheta}_{g+}$

C. Adaptation Laws

The proposed algorithms for estimating the positive-sequence angle $\hat{\vartheta}_{g+}$, magnitude $\hat{u}_{g+}$, and frequency $\hat{\omega}_{g+}$ are based on the small-signal linearized model (14). The estimator for the positive-sequence angle is given in (7), and the estimator for the positive-sequence magnitude is

$$\hat{u}_{g+}(z) = \underbrace{\frac{k_{i,u}}{z-1}}_{F_u(z)} \mathrm{Re}\left\{\frac{\boldsymbol{a}_1}{\boldsymbol{b}_1}e^{j\phi}\tilde{\boldsymbol{i}}_c(z)\right\} \tag{18}$$

where $k_{i,u}$ is the gain, and ϕ, $\boldsymbol{a}_1$, and $\boldsymbol{b}_1$ are explained at the end of this subsection. The estimator for the angular frequency is

$$\hat{\omega}_{g+}(z) = \frac{1}{u_{g+,0}} \underbrace{\left(k_{p,\omega} + \frac{k_{i,\omega}}{z-1}\right)}_{F_\omega(z)} \mathrm{Im}\left\{\frac{\boldsymbol{a}_1}{\boldsymbol{b}_1}e^{j\phi}\tilde{\boldsymbol{i}}_c(z)\right\} \tag{19}$$

where $u_{g+,0}$ is the positive-sequence voltage at the operating point, and $k_{p,\omega}$ and $k_{i,\omega}$ are the estimator gains. Furthermore, the integral part of (19) provides a naturally filtered frequency estimate, e.g., for monitoring purposes [19]

$$\hat{\omega}_{gf}(z) = \frac{1}{u_{g+,0}} \frac{k_{i,\omega}}{z-1} \mathrm{Im}\left\{\frac{\boldsymbol{a}_1}{\boldsymbol{b}_1}e^{j\phi}\tilde{\boldsymbol{i}}_c(z)\right\} \tag{20}$$

The constants ϕ, $\boldsymbol{a}_1$, and $\boldsymbol{b}_1$ are obtained from the quasi-steady-state analysis of the linearized model, as explained in [19]. These constants describe the steady-state gain from $\tilde{u}_{g+}$ and $\tilde{\vartheta}_{g+}$ to $\tilde{\boldsymbol{i}}_c$ as follows

$$\tilde{\boldsymbol{i}}_c = \underbrace{e^{-j\phi}(\boldsymbol{b}_1/\boldsymbol{a}_1)}_{\boldsymbol{G}_{iu}(1)}\tilde{u}_{g+} + \underbrace{ju_{g0}e^{-j\phi}(\boldsymbol{b}_1/\boldsymbol{a}_1)}_{\boldsymbol{G}_{i\vartheta}(1)}\tilde{\vartheta}_{g+} \tag{21}$$

and they are obtained by making $z = 1$ in (15) and (17). The constants are

$$\begin{aligned}
\phi &= (3/2)\omega_{g+}T_s \\
\boldsymbol{a}_1 &= \omega_{g+}C_f L_{fc} L_{fg}(\omega_{g+}^2 - \omega_p^2) \\
&\quad \cdot (1-\boldsymbol{\alpha}_{o1})(1-\boldsymbol{\alpha}_{o2})(1-\boldsymbol{\alpha}_{o3})(1-\boldsymbol{\alpha}_{o4}) \\
\boldsymbol{b}_1 &= 4(1-e^{-2j\omega_{g+}T_s})\sin(\omega_{g+}T_s/2) \\
&\quad \cdot [\cos(\omega_{g+}T_s) - \cos(\omega_p T_s)]
\end{aligned} \tag{22}$$

where $\omega_p = \sqrt{(L_{fc}+L_{fg})/(C_f L_{fc} L_{fg})}$ is the resonance frequency of the LCL filter and $\boldsymbol{\alpha}_{o1}$, $\boldsymbol{\alpha}_{o2}$, $\boldsymbol{\alpha}_{o3}$, and $\boldsymbol{\alpha}_{o4}$ are the discrete-time poles (tuning parameters) of the state observer.

TABLE I
SYSTEM PARAMETERS

Param.	Value	Param.	Value
u_g	$\sqrt{2/3}\cdot 400$ V (1 p.u.)	L_{fc}	3.3 mH (0.081 p.u.)
ω_{g+}	$2\pi \cdot 50$ rad/s (1 p.u.)	L_{fg}	3.0 mH (0.074 p.u.)
i_N	$\sqrt{2}\cdot 18$ A (1 p.u.)	C_f	8.8 μF (0.036 p.u.)
f_{sw}	4 kHz	T_s	$1/(2f_{sw}) = 125$ μs

D. Tuning of the Observer

The proposed observer is tuned based on direct pole placement. Two sets of poles are placed: poles of the state observer and poles of the adaptation loops.

1) Poles of the State Observer: The gain $\mathbf{K}_o$ is calculated by selecting the pole locations of the augmented state observer. These poles are the roots of (16). Four complex poles $\boldsymbol{\alpha}_{o1} \ldots \boldsymbol{\alpha}_{o4}$ can be placed resulting in the desired characteristic polynomial

$$\boldsymbol{a}(z) = (z-\boldsymbol{\alpha}_{o1})(z-\boldsymbol{\alpha}_{o2})(z-\boldsymbol{\alpha}_{o3})(z-\boldsymbol{\alpha}_{o4}) \tag{23}$$

Analytical expressions for the observer gain $\mathbf{K}_o$ are calculated by equalizing (16) and (23). The resulting expressions are functions of $\boldsymbol{\alpha}_{o1} \ldots \boldsymbol{\alpha}_{o4}$ and the elements of $\mathbf{\Phi}_a$.

In order to simplify the selection of the pole locations, the discrete-time poles are mapped via the continuous-time polynomials $(s^2 + 2\zeta_{od}\omega_{od}s + \omega_{od}^2)(s^2 + 2\zeta_{or}\omega_{or}s + \omega_{or}^2)$ resulting in

$$\begin{aligned}
\boldsymbol{\alpha}_{o1,2} &= \exp[(-\zeta_{od} \pm j\sqrt{1-\zeta_{od}^2})\omega_{od}T_s] \\
\boldsymbol{\alpha}_{o3,4} &= \exp[(-\zeta_{or} \pm j\sqrt{1-\zeta_{or}^2})\omega_{or}T_s]
\end{aligned} \tag{24}$$

where the natural frequencies (ω_{od}, ω_{or}) and damping ratios (ζ_{od}, ζ_{or}) determine the location of the poles. Following the direct pole-placement principle proposed in [25], the natural frequency ω_{od} is here set twice as fast as the bandwidth of current control. The natural frequency ω_{or} is set to the resonance frequency of the LCL filter, i.e., $\omega_{or} = \omega_p$. It is to be noted that this selection is a practical example, and a designer has the full freedom to change the pole locations depending on the dynamic performance specifications and conditions. In other words, dynamic behavior and robustness against parameter errors are related to the location of the poles. For example, if the measured current $\boldsymbol{i}_c$ is noisy, the natural frequencies can be reduced in order to increase measurement-noise rejection and robustness. Alternatively, the natural frequencies of the poles can be increased if a faster dynamic response is desired.

2) Poles of the Adaptation Loops: Since the adaptation mechanisms are slow in comparison with the state observer, the quasi-steady-state approximation (21) of the linearized dynamics can be used for tuning of the positive-sequence magnitude, frequency, and angle estimators. The estimators (7), (18), (19) form loops together with (21), as shown in Fig. 4. The gains for the estimators are calculated by selecting the pole locations of these closed adaptation loops. The resulting gain of the positive-sequence magnitude estimator is

$$k_{i,u} = 1 - \exp(-\omega_u T_s) \tag{25}$$

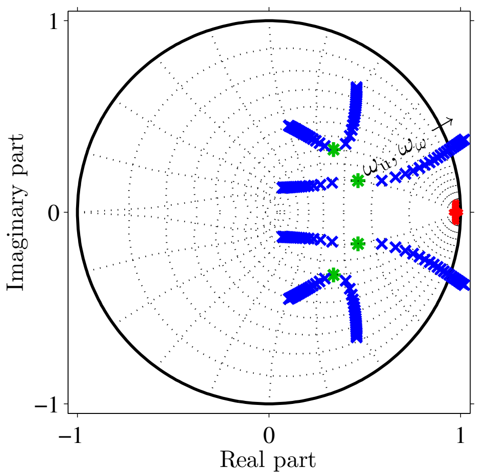

Fig. 5. Root loci of the poles of the linearized system (27), when ω_u and ω_ω are increased from $2\pi \cdot 5$ rad/s to $2\pi \cdot 100$ rad/s. The state-observer poles are marked with blue x and their original location is marked with green *. The slow-frequency poles of the adaptation loops, determined by ω_u and ω_ω, are in red.

where ω_u is the natural frequency of the pole of the magnitude-estimation loop. Furthermore, the gains of the angle-estimation loops become

$$\begin{aligned} k_{\mathrm{p},\omega} &= 2[1 - \exp(-\zeta_\omega \omega_\omega T_\mathrm{s}) \cos(\sqrt{1-\zeta_\omega^2}\omega_\omega T_\mathrm{s})]/T_\mathrm{s} \\ k_{\mathrm{i},\omega} &= [\exp(-2\zeta_\omega \omega_\omega T_\mathrm{s}) - 1]/T_\mathrm{s} + k_{\mathrm{p},\omega} \end{aligned} \tag{26}$$

where ω_ω is the natural frequency and ζ_ω is the damping ratio of the complex pole pair of the angle-estimation loop.

The natural frequencies ω_u and ω_ω and the damping ratio ζ_ω are the tuning parameters of the loops, and the natural frequencies can be thought as approximate bandwidths. It is worth noticing that the linearized system [(15) and (17)] has a zero ($z = \mathrm{e}^{-2\mathrm{j}\omega_{\mathrm{g}+} T_\mathrm{s}}$) at the unit circle[2] that limits the maximum values of ω_u and ω_ω.

IV. Stability and Estimation Error Analyses

A. Small-Signal Stability

The small-signal stability of the proposed observer is analyzed in the nominal operation point. In the stability analysis, $\tilde{u}_{\mathrm{g}+}(k) = u_{\mathrm{g}+}(k) - \hat{u}_{\mathrm{g}+}(k)$, $\tilde{\omega}_\mathrm{gf}(k) = \omega_{\mathrm{g}+}(k) - \hat{\omega}_\mathrm{gf}(k)$, and $\tilde{\omega}_{\mathrm{g}+}(k) = \omega_{\mathrm{g}+}(k) - \hat{\omega}_{\mathrm{g}+}(k)$, where $u_{\mathrm{g}+}$ and $\omega_{\mathrm{g}+}$ as external disturbances can be set to zero. Considering (9), (13), and (18)–(20), the small-signal model for the closed-loop system is obtained as follows

$$\begin{cases} \tilde{\mathbf{x}}_\mathrm{a}(k+1) = (\mathbf{\Phi}_\mathrm{a} - \mathbf{K}_\mathrm{o}\mathbf{C}_\mathrm{a})\tilde{\mathbf{x}}_\mathrm{a}(k) + \mathbf{\Gamma}_\mathrm{ga}\tilde{u}_{\mathrm{g}+}(k) \\ \qquad\qquad + \mathrm{j}\mathbf{\Gamma}_\mathrm{ga} u_{\mathrm{g}+,0}\tilde{\vartheta}_{\mathrm{g}+}(k) + \mathbf{\Gamma}_\omega \tilde{\omega}_{\mathrm{g}+}(k) \\ \tilde{u}_{\mathrm{g}+}(k+1) = \tilde{u}_{\mathrm{g}+}(k) - k_{\mathrm{i,u}} \operatorname{Re}\left\{ \dfrac{\boldsymbol{a}_1}{\boldsymbol{b}_1} \mathrm{e}^{\mathrm{j}\phi} \mathbf{C}_\mathrm{a}\tilde{\mathbf{x}}_\mathrm{a}(k) \right\} \\ \tilde{\omega}_\mathrm{gf}(k+1) = \tilde{\omega}_\mathrm{gf}(k) - \dfrac{k_{\mathrm{i},\omega}}{u_{\mathrm{g}+,0}} \operatorname{Im}\left\{ \dfrac{\boldsymbol{a}_1}{\boldsymbol{b}_1} \mathrm{e}^{\mathrm{j}\phi} \mathbf{C}_\mathrm{a}\tilde{\mathbf{x}}_\mathrm{a}(k) \right\} \\ \tilde{\vartheta}_{\mathrm{g}+}(k+1) = \tilde{\vartheta}_{\mathrm{g}+}(k) + T_\mathrm{s}\tilde{\omega}_{\mathrm{g}+}(k) \end{cases} \tag{27}$$

[2]This corresponds to an imaginary-axis zero in continuous time. In other words, the zero is in the closed right-half plane, which limits the bandwidth of the system [26].

where

$$\tilde{\omega}_{\mathrm{g}+}(k) = -\frac{k_{\mathrm{p},\omega}}{u_{\mathrm{g}+,0}} \operatorname{Im}\left\{ \frac{\boldsymbol{a}_1}{\boldsymbol{b}_1} \mathrm{e}^{\mathrm{j}\phi} \tilde{\boldsymbol{i}}(k) \right\} + \tilde{\omega}_\mathrm{gf}(k) \tag{28}$$

A numerical example of the observer tuning is presented. The system parameters are given in Table I. The tuning parameters of the state observer are: $\omega_\mathrm{od} = 2\pi \cdot 1000$ rad/s, $\omega_\mathrm{or} = \omega_\mathrm{p}$, $\zeta_\mathrm{od} = 0.9$, and $\zeta_\mathrm{or} = 0.7$. Fig. 5 shows the poles of the closed-loop system (27), when ω_u is increased from $2\pi \cdot 5$ rad/s to $2\pi \cdot 100$ rad/s, $\omega_\omega = \omega_\mathrm{u}$, and $\zeta_\omega = 1$. The adaptation mechanisms change the original location of the state-observer poles determined by $\mathbf{K}_\mathrm{o}$. Two state observer poles drift outside of the stable region (unit circle) when $\omega_\mathrm{u} = \omega_\omega > 2\pi \cdot 65$ rad/s. On the other hand, when $\omega_\mathrm{u} = \omega_\omega < 2\pi \cdot 35$ rad/s, the damping ratios of the all poles are greater than 0.4. This means that the estimation-error dynamics have a reasonable damping. Moreover, with $\omega_\mathrm{u} = \omega_\omega \geq 2\pi \cdot 35$ rad/s, the 5-% settling times for the estimation errors of the grid-voltage magnitude and angle are fast (less than a 20-ms fundamental cycle of the voltage) for a step change in the actual grid-voltage magnitude or angle [19].

At the equilibrium point, when the linearized sytem is strictly stable or unstable, the actual nonlinear system is also locally stable or unstable, respectively [27]. However, the local stability cannot guarantee the global stability, and the linerized model does not necessary describe the behaviour of the system for large deviations from the equilibrium point. Nevertheless, the information obtained from the small-signal analysis is important for understanding limitations of the system. More information is acquired by means of computer simulations and experiments.

B. Steady-State Estimation Errors

The stability analysis of Section IV-A is accurate with the accurate circuit parameters ($\hat{L}_\mathrm{fc} = L_\mathrm{fc}$, $\hat{C}_\mathrm{f} = C_\mathrm{f}$, $\hat{L}_\mathrm{fg} = L_\mathrm{fg}$), i.e., when the steady-state estimation errors are zero ($\tilde{\mathbf{x}}_\mathrm{a0} = \mathbf{0}, \tilde{u}_{\mathrm{g}+,0} = 0, \tilde{\omega}_{\mathrm{g}+,0} = 0, \tilde{\vartheta}_{\mathrm{g}+,0} = 0$). In real applications, the circuit parameters of the LCL filter have some manufacturing tolerances or uncertainties. Hence, the model parameters in the observer are erroneous ($\hat{L}_\mathrm{fc} \neq L_\mathrm{fc}$, $\hat{C}_\mathrm{f} \neq C_\mathrm{f}$, and $\hat{L}_\mathrm{fg} \neq L_\mathrm{fg}$). Then, the steady-state estimation errors $\tilde{\mathbf{x}}_\mathrm{a0}$, $\tilde{u}_{\mathrm{g}+,0}$, $\tilde{\vartheta}_{\mathrm{g}+,0}$ are not necessarily zero. Nevertheless, the steady-state estimation error of the converter current $\tilde{\boldsymbol{i}}_\mathrm{c0}$ is zero, since the integrators of the adaptation mechanisms drive $\tilde{\boldsymbol{i}}_\mathrm{c}$ to zero. In addition, the estimation error of the angular frequency $\tilde{\omega}_{\mathrm{g}+}$ is zero in steady state, which originates from the steady-state condition $\tilde{\vartheta}_{\mathrm{g}+}(k+1) = \tilde{\vartheta}_{\mathrm{g}+}(k)$, cf. (9).

Since the steady-state feedback signal of the observer is $\tilde{\boldsymbol{i}}_\mathrm{c0} = 0$, the steady-state estimation errors $\tilde{\mathbf{x}}_\mathrm{a0}$, $\tilde{u}_{\mathrm{g}+,0}$, $\tilde{\vartheta}_{\mathrm{g}+,0}$ do not depend on the observer and adaptation loop gains $\mathbf{K}_\mathrm{o}$, $k_\mathrm{i,u}$, $k_{\mathrm{p},\omega}$, and $k_{\mathrm{i},\omega}$. These errors originate from: 1) parameter errors $\tilde{L}_\mathrm{fc} = L_\mathrm{fc} - \hat{L}_\mathrm{fc}$, $\tilde{C}_\mathrm{f} = C_\mathrm{f} - \hat{C}_\mathrm{f}$, and $\tilde{L}_\mathrm{fg} = L_\mathrm{fg} - \hat{L}_\mathrm{fg}$; 2) unmodeled series resistances R_fc, R_f, and R_fg of L_fc, C_f, and L_fg, respectively; and 3) other unmodeled phenomena and parasitic components.

It is worth noticing that all model-based grid-voltage estimation methods result in a biased grid-voltage estimate in steady state, if the model has inaccuracies. The estimation

TABLE II
OBSERVER TUNING PARAMETERS

Parameter	Value	Parameter	Value
ω_{od}	$2\pi \cdot 1000$ rad/s	ζ_{od}	0.9
ω_{or}	ω_{p}	ζ_{or}	0.7
$\omega_{\mathrm{u}} = \omega_{\omega}$	$2\pi \cdot 25$ rad/s	ζ_{ω}	1

accuracy could be increased if estimated resistive components were included in the observer (as in [8], [13], [18], [28]). Then, the pole placement of the observer would also be more accurate, improving the control performance [28]. However, a drawback of the modeled resistances is the increased number of parameters that should be determined or estimated in the design stage. Moreover, at high power ratings, the effects of the parasitic resistances on the estimation errors are less significant, since the per-unit losses of an LCL filter typically decrease when the power rating of the system increases. Furthermore, to increase estimation accuracy, saturation of the inductors could be modeled [29].

Let us examine steady-state magnitude error $\tilde{u}_{\mathrm{g}+,0}$ and angle error $\tilde{\vartheta}_{\mathrm{g}+,0}$, in the operating conditions where the converter is injecting a positive-sequence current to the grid. In the positive-sequence coordinates, the converter current is $\boldsymbol{i}^{\mathrm{p}}_{\mathrm{c0}}$ and the grid voltage components are $u_{\mathrm{g}+,0}$, and $\boldsymbol{u}^{\mathrm{p}}_{\mathrm{g}-,0}$. Then, the other signals, such as $\boldsymbol{u}^{\mathrm{p}}_{\mathrm{c0}}$, can be solved from the true LCL circuit, cf. Fig. 1(a), or from (3). Once $\boldsymbol{u}^{\mathrm{p}}_{\mathrm{c0}}$ and $\hat{\boldsymbol{i}}^{\mathrm{p}}_{\mathrm{c0}} = \boldsymbol{i}^{\mathrm{p}}_{\mathrm{c0}}$ are known, the estimated grid voltage $\hat{\boldsymbol{u}}^{\mathrm{p}}_{\mathrm{g}+,0}$ in the positive-sequence coordinates can be calculated from the LCL circuit [Fig. 1(a)] or from (8) using the estimated parameters ($\hat{L}_{\mathrm{fc}}$, $\hat{C}_{\mathrm{f}}$, $\hat{L}_{\mathrm{fg}}$). Furthermore, to get a rough estimate of the parameter sensitivity, the calculation can be simplified by approximating

$$\hat{\boldsymbol{u}}^{\mathrm{p}}_{\mathrm{g}+,0} \approx u_{\mathrm{g}+,0} + \left[\mathrm{j}\omega_{\mathrm{g}+}(\tilde{L}_{\mathrm{fc}} + \tilde{L}_{\mathrm{fg}}) + R_{\mathrm{fc}} + R_{\mathrm{fg}}\right] \boldsymbol{i}^{\mathrm{p}}_{\mathrm{c0}} \quad (29)$$

where the fundamental-frequency current of the capacitor branch is assumed to be zero. Finally, the steady-state angle error is $\tilde{\vartheta}_{\mathrm{g}+,0} = -\angle \hat{\boldsymbol{u}}^{\mathrm{p}}_{\mathrm{g}+,0}$ and the magnitude error is $\tilde{u}_{\mathrm{g}+,0} = u_{\mathrm{g}+,0} - |\hat{\boldsymbol{u}}^{\mathrm{p}}_{\mathrm{g}+,0}|$.

The simplified expression (29) shows that an active-power producing current component, e.g., $\boldsymbol{i}^{\mathrm{p}}_{\mathrm{c0}} = i_{\mathrm{cd}} + \mathrm{j}0$, produces a steady-state angle error, if there is an error in the inductances of the observer. Moreover, with some parasitic resistance (R_{fc} or R_{fg}), $\boldsymbol{i}^{\mathrm{p}}_{\mathrm{c0}} = i_{\mathrm{cd}} + \mathrm{j}0$ produces a steady-state magnitude estimation error. With a reactive-power producing current component, e.g., $\boldsymbol{i}^{\mathrm{p}}_{\mathrm{c0}} = 0 + \mathrm{j}i_{\mathrm{cq}}$, the result is opposite.

In order to study local stability in the case of erroneous parameters in the observer, the nonlinear estimation-error dynamics (12) could be linearized at an equilibrium point determined by nonzero steady-state estimation errors. Since the steady-state estimation errors depend on the operating point of the converter system, the nonlinear dynamics should be linearized at various operating points. The detailed small-signal analysis under parameter errors becomes laborious. Alternatively, stability and dynamic performance of the observer under parameter errors is examined with computer simulations in Section V.

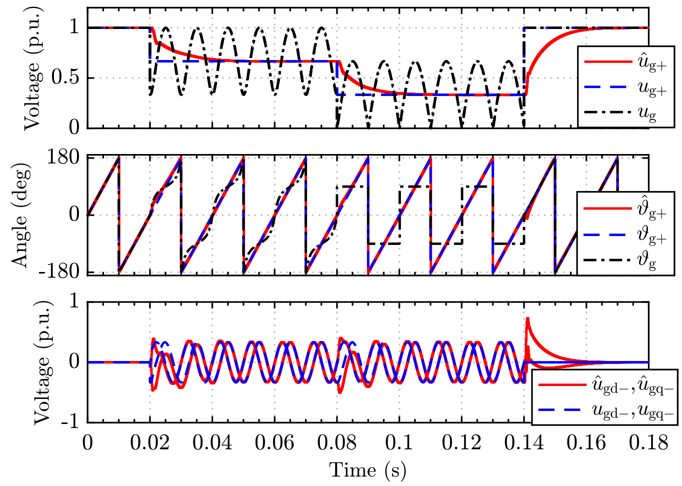

Fig. 6. Simulated waveforms in different grid-voltage conditions. The first subplot shows the estimated magnitude (solid) and actual magnitude (dashed) of the positive-sequence voltage, and actual magnitude of the grid-voltage vector (dash-dotted). The second subplot shows the estimated angle (solid) and actual angle (dashed) of the positive-sequence voltage, and actual angle of the grid-voltage vector (dash-dotted). The third subplot shows the estimated (solid) and actual (dashed) negative-sequence voltages $\hat{\boldsymbol{u}}_{\mathrm{g}-} = \hat{u}_{\mathrm{gd}-} + \mathrm{j}\hat{u}_{\mathrm{gq}-}$ and $\boldsymbol{u}_{\mathrm{g}-} = u_{\mathrm{gd}-} + \mathrm{j}u_{\mathrm{gq}-}$, respectively.

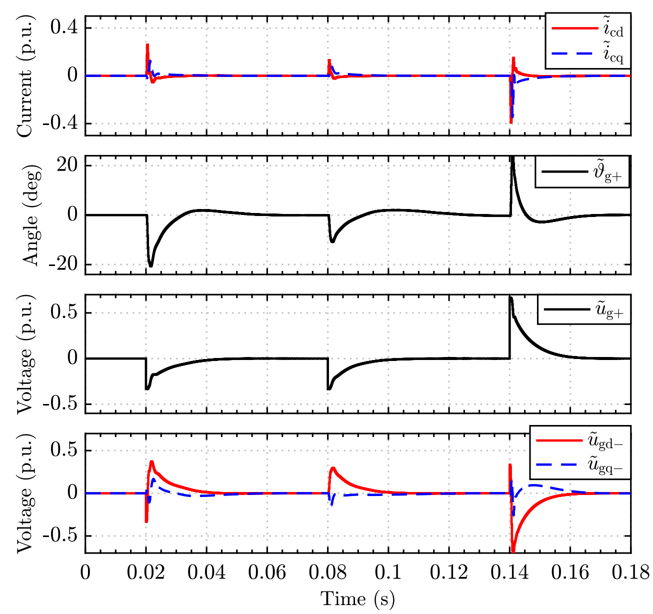

Fig. 7. Simulated waveforms in different grid-voltage conditions: (first) converter current estimation error; (second) positive-sequence angle estimation error; (third) positive-sequence magnitude estimation error; (fourth) negative-sequence estimation error $\tilde{\boldsymbol{u}}_{\mathrm{g}-} = \tilde{u}_{\mathrm{gd}-} + \mathrm{j}\tilde{u}_{\mathrm{gq}-}$.

V. SIMULATION RESULTS

The proposed observer is first tested simulating it in parallel with a current-controlled converter. The parallel operation separates the dynamic behavior of the observer from the dynamic behavior of the control system. The nominal model parameters, given in Table I, are used in the observer. The observer tuning parameters are given in Table II. Corresponding tuning parameters were used in the stability analysis in Section IV-A.

A. Validation

Figs. 6 and 7 show simulated waveforms under the following grid-voltage conditions: 1) symmetrical and nominal grid conditions; 2) positive-sequence magnitude drops down to 2/3 p.u. and negative-sequence magnitude steps up to 1/3 p.u.; 3) positive-sequence magnitude drops down to 1/3 p.u. and the negative sequence magnitude is not changed; 4) symmetrical grid conditions. During the test, the converter current is controlled to $\boldsymbol{i}_{\mathrm{c}} = 1 + \mathrm{j}0$ p.u., and the system parameters are nominal, cf. Table I.

Fig. 6 shows the estimated and actual positive-sequence magnitudes and angles during the test sequence. The figure also shows the actual magnitude $u_{\mathrm{g}} = |\boldsymbol{u}_{\mathrm{g}}^{\mathrm{s}}|$ and angle $\vartheta_{\mathrm{g}} = \angle\boldsymbol{u}_{\mathrm{g}}^{\mathrm{s}}$ of the grid-voltage vector. Furthermore, the real and imaginary parts of the actual negative-sequence voltage ($\boldsymbol{u}_{\mathrm{g}-} = u_{\mathrm{gd}-} + \mathrm{j}u_{\mathrm{gq}-}$) and the estimated negative-sequence voltage ($\hat{\boldsymbol{u}}_{\mathrm{g}-} = \hat{u}_{\mathrm{gd}-} + \mathrm{j}\hat{u}_{\mathrm{gq}-}$) are shown. The estimated values converge to the actual values approximatively in a 20-ms grid-voltage cycle. This is more clearly visible in Fig. 7 that shows estimation-error responses of the converter current, angle and magnitude of the positive-sequence voltage, and d and q-components of the negative-sequence voltage. Moreover, the steady-state estimation error of these signals is zero, since the parameters inside the observer matrices equal true circuit parameters ($\hat{L}_{\mathrm{fc}} = L_{\mathrm{fc}}$, $\hat{C}_{\mathrm{f}} = C_{\mathrm{f}}$, and $\hat{L}_{\mathrm{fg}} = L_{\mathrm{fg}}$). This result agrees with the theory and demonstrates that the small-signal linearization around the equilibrium point $\{\tilde{\mathbf{x}}_{\mathrm{a0}} = \mathbf{0}, \tilde{u}_{\mathrm{g+,0}} = 0, \tilde{\omega}_{\mathrm{g+,0}} = 0, \tilde{\vartheta}_{\mathrm{g+,0}} = 0\}$ is valid. The convergence rate of the voltage angle and magnitude estimation errors corresponds the designed dynamics of the adaptation loops (with $\omega_{\mathrm{u}} = \omega_{\omega} = 2\pi \cdot 25$ rad/s, the theoretical 5% settling times for $\tilde{u}_{\mathrm{g}}$ and $\tilde{\vartheta}_{\mathrm{g+}}$ are 19 ms and 27 ms, respectively [19]). Interestingly, similar settling times have also been reported for virtual-flux based estimation methods [30]. The faster dynamics in $\tilde{\boldsymbol{i}}_{\mathrm{c}}$ originate from the poles of the state observer at $\omega_{\mathrm{od}} = 2\pi \cdot 1000$ rad/s and $\omega_{\mathrm{or}} = \omega_{\mathrm{p}}$.

B. Parameter Errors

The model parameters in the observer may be erroneous ($\hat{L}_{\mathrm{fc}} \neq L_{\mathrm{fc}}$, $\hat{C}_{\mathrm{f}} \neq C_{\mathrm{f}}$, and $\hat{L}_{\mathrm{fg}} \neq L_{\mathrm{fg}}$). The parameter sensitivity of the proposed observer is studied simulating the observer in various conditions and with different parameter errors. Fig. 8 shows estimation error responses when the true circuit parameters are $L_{\mathrm{fc}} = 2\hat{L}_{\mathrm{fc}}$, $C_{\mathrm{f}} = 2\hat{C}_{\mathrm{f}}$, and $L_{\mathrm{fg}} = 2\hat{L}_{\mathrm{fg}}$. Fig. 9 shows the same responses when $L_{\mathrm{fc}} = 0.5\hat{L}_{\mathrm{fc}}$, $C_{\mathrm{f}} = 0.5\hat{C}_{\mathrm{f}}$, and $L_{\mathrm{fg}} = 0.5\hat{L}_{\mathrm{fg}}$. The operating point of the converter current is $\boldsymbol{i}_{\mathrm{c}}^{\mathrm{p}} = 1 + \mathrm{j}0$ p.u. and the positive- and negative-sequence components of the grid-voltage equal those of the test sequence in Section V-A and Fig. 6.

As Figs. 8 and 9 show, under the parameter errors, the observer remains stable and the convergence rate of the estimated quantities is similar in comparison with the case of accurate parameters shown in Fig. 7. However, the effective damping of the estimation error dynamics is lower with erroneous parameters, which can be seen as a high-frequency oscillation in the transient responses. Moreover, when the observer parameters differ from the true circuit parameters, the steady-state errors

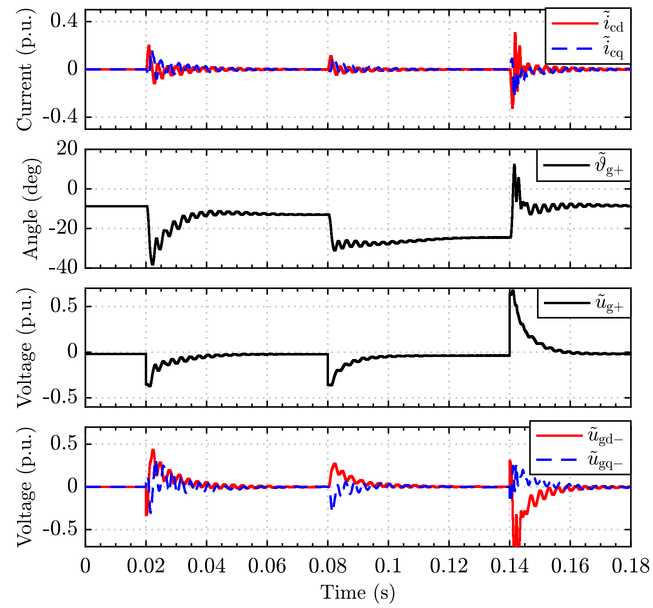

Fig. 8. Simulated waveforms when $L_{\mathrm{fc}} = 2\hat{L}_{\mathrm{fc}}$, $C_{\mathrm{f}} = 2\hat{C}_{\mathrm{f}}$, and $L_{\mathrm{fg}} = 2\hat{L}_{\mathrm{fg}}$: (first) converter current estimation error; (second) positive-sequence angle estimation error; (third) positive-sequence magnitude estimation error; (fourth) negative-sequence estimation error $\tilde{\boldsymbol{u}}_{\mathrm{g}-} = \tilde{u}_{\mathrm{gd}-} + \mathrm{j}\tilde{u}_{\mathrm{gq}-}$.

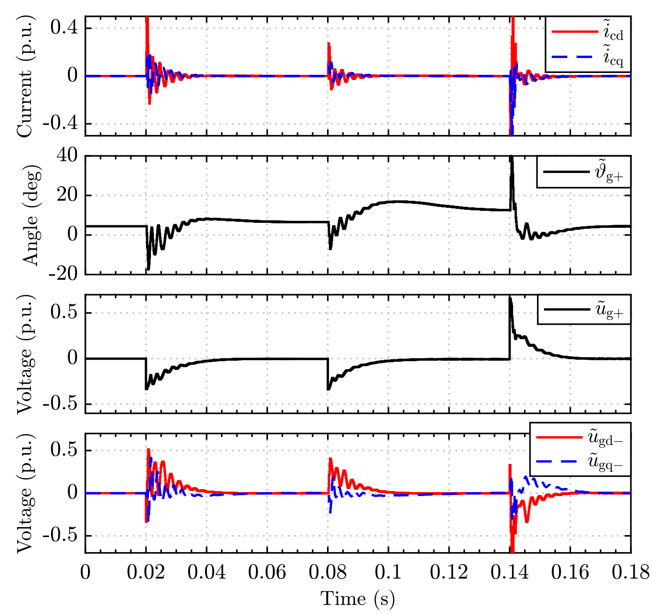

Fig. 9. Simulated waveforms when $L_{\mathrm{fc}} = 0.5\hat{L}_{\mathrm{fc}}$, $C_{\mathrm{f}} = 0.5\hat{C}_{\mathrm{f}}$, and $L_{\mathrm{fg}} = 0.5\hat{L}_{\mathrm{fg}}$: (first) converter current estimation error; (second) positive-sequence angle estimation error; (third) positive-sequence magnitude estimation error; (fourth) negative-sequence estimation error $\tilde{\boldsymbol{u}}_{\mathrm{g}-} = \tilde{u}_{\mathrm{gd}-} + \mathrm{j}\tilde{u}_{\mathrm{gq}-}$.

of the estimated positive-sequence angle and magnitude are nonzero. The simulated steady-state errors are given in Table III in two different operating points. The cases 2LCL and 0.5LCL in the table refer to the simulations where $L_{\mathrm{fc}} = 2\hat{L}_{\mathrm{fc}}$, $C_{\mathrm{f}} = 2\hat{C}_{\mathrm{f}}$, and $L_{\mathrm{fg}} = 2\hat{L}_{\mathrm{fg}}$ and $L_{\mathrm{fc}} = 0.5\hat{L}_{\mathrm{fc}}$, $C_{\mathrm{f}} = 0.5\hat{C}_{\mathrm{f}}$, and $L_{\mathrm{fg}} = 0.5\hat{L}_{\mathrm{fg}}$, respectively. The table also shows theoretical errors calculated using (29). The simulated steady-state errors match well with the calculated errors even though (29) is approximative and neglects the capacitor branch of the LCL

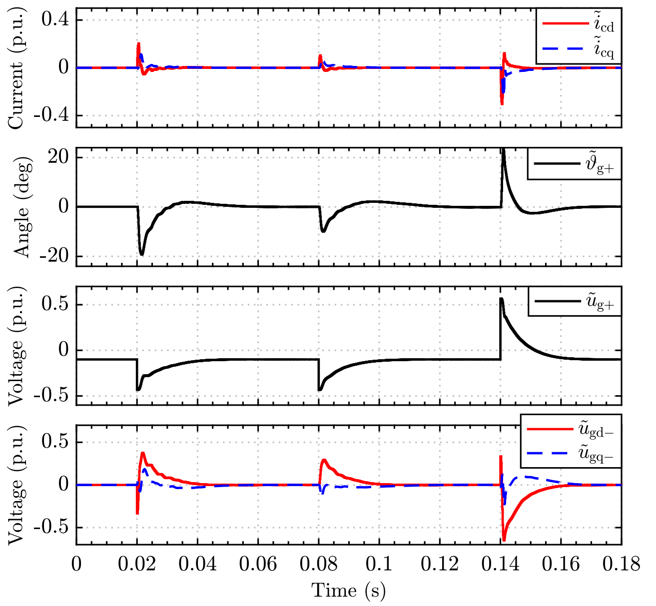

Fig. 10. Simulated waveforms when $R_{\mathrm{fc}} = R_{\mathrm{fg}} = 0.05$ p.u. and $R_{\mathrm{f}} = 1$ p.u.: (first) converter current estimation error; (second) positive-sequence angle estimation error; (third) positive-sequence magnitude estimation error; (fourth) negative-sequence estimation error $\tilde{\boldsymbol{u}}_{\mathrm{g}-} = \tilde{u}_{\mathrm{gd}-} + \mathrm{j}\tilde{u}_{\mathrm{gq}-}$.

TABLE III
STEADY-STATE ESTIMATION ERRORS

Operating point: $\boldsymbol{i}_{\mathrm{c0}}^{\mathrm{P}} = 1 + \mathrm{j}0$ p.u. and $u_{\mathrm{g+,0}} = 1$ p.u.

Case	Simulation $\tilde{u}_{\mathrm{g+,0}}$ (p.u.)	Simulation $\tilde{\vartheta}_{\mathrm{g+,0}}$ (deg)	Calculation (29) $\tilde{u}_{\mathrm{g+,0}}$ (p.u.)	Calculation (29) $\tilde{\vartheta}_{\mathrm{g+,0}}$ (deg)
2LCL	−0.019	−8.76	−0.012	−8.77
0.5LCL	−0.001	4.42	−0.003	4.41
R	−0.10	0.093	−0.10	0.00

Operating point: $\boldsymbol{i}_{\mathrm{c0}}^{\mathrm{P}} = 1 + \mathrm{j}0$ p.u. and $u_{\mathrm{g+,0}} = 1/3$ p.u.

Case	Simulation $\tilde{u}_{\mathrm{g+,0}}$ (p.u.)	Simulation $\tilde{\vartheta}_{\mathrm{g+,0}}$ (deg)	Calculation (29) $\tilde{u}_{\mathrm{g+,0}}$ (p.u.)	Calculation (29) $\tilde{\vartheta}_{\mathrm{g+,0}}$ (deg)
2LCL	−0.037	−24.8	−0.034	−24.8
0.5LCL	−0.008	13.1	−0.009	13.0
R	−0.10	0.086	−0.10	0.00

filter.

Fig. 10 shows simulated estimation error responses when the LCL filter inductances and capacitance are nominal both in the real circuit and the observer, but the real LCL filter has series resistances $R_{\mathrm{fc}} = R_{\mathrm{fg}} = 0.05$ p.u. in the inductors and $R_{\mathrm{f}} = 1$ p.u. in the capacitor branch. Again the observer remains stable and the convergence of the estimated quantities is almost identical in comparison with the case without resistances shown in Fig. 7. However, the steady-state estimation error of the positive-sequence magnitude is -0.1 p.u. when there are the resistances in the circuit. This steady-state error can be predicted theoretically using (29) as Table III shows (case R). Moreover, the steady-state angle estimation error is minor in this case as shown in the table. Nevertheless, the steady-state estimation errors could be reduced with a more accurate system model as explained in Section IV-B.

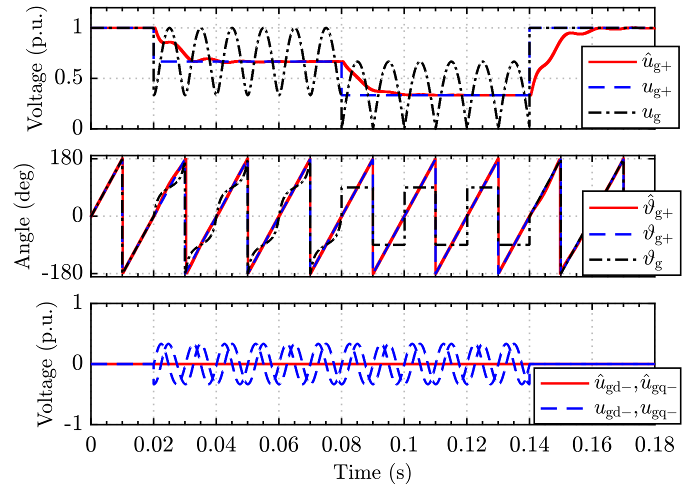

Fig. 11. Simulated waveforms of the observer proposed in [19] in different grid-voltage conditions. The first subplot shows the estimated magnitude (solid) and actual magnitude (dashed) of the positive-sequence voltage, and actual magnitude of the grid-voltage vector (dash-dotted). The second subplot shows the estimated angle (solid) and actual angle (dashed) of the positive-sequence voltage, and actual angle of the grid-voltage vector (dash-dotted). The third subplot shows the estimated (solid) and actual (dashed) negative-sequence voltage components.

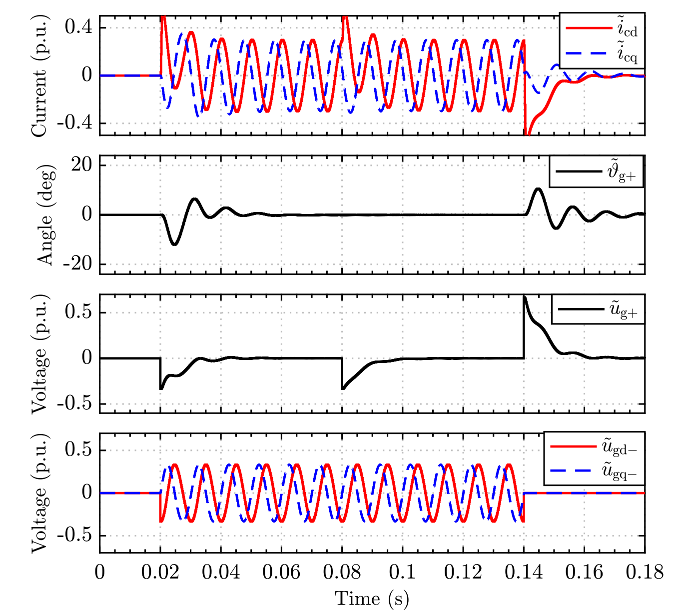

Fig. 12. Simulated waveforms of the observer proposed in [19] in different grid-voltage conditions: (first) converter current estimation error; (second) positive-sequence angle estimation error; (third) positive-sequence magnitude estimation error; (fourth) negative-sequence estimation error $\tilde{\boldsymbol{u}}_{\mathrm{g}-} = \tilde{u}_{\mathrm{gd}-} + \mathrm{j}\tilde{u}_{\mathrm{gq}-}$.

C. Comparison

The dynamic performance of the proposed observer is compared with the observer proposed in [19]. The reference observer [19] was simulated in the same grid conditions and operating points described in Section V-A. The tuning parameters of the reference observer were set according to Table II in order to ensure fair comparison. A notch filter for the negative sequence was used with the reference observer as described in [19].

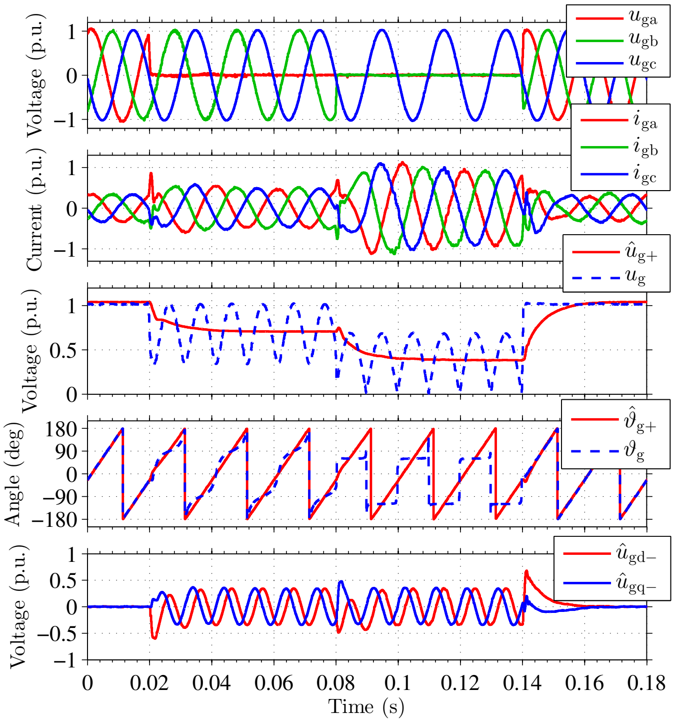

Fig. 13. Measured waveforms in different grid-voltage conditions: (first) grid voltages; (second) grid currents; (third) estimated positive-sequence magnitude (solid) and actual magnitude of the grid-voltage vector (dashed); (fourth) estimated positive-sequence angle (solid) and actual angle of the grid-voltage vector (dashed); and (fifth) estimated negative-sequence components.

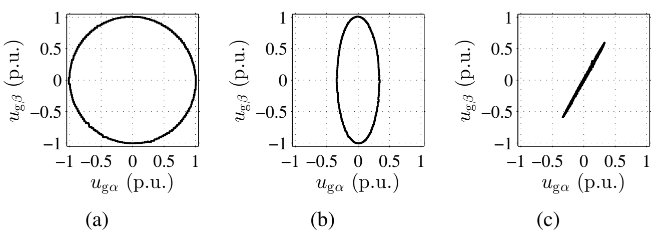

Fig. 14. Measured locus of the grid-voltage space vector $\boldsymbol{u}_{\mathrm{g}}^{\mathrm{s}} = u_{\mathrm{g}\alpha} + \mathrm{j}u_{\mathrm{g}\beta}$: (a) symmetrical conditions; (b) the measured vector rotates an elliptic orbit when the single-phase dip is applied; and (c) the rotation stops (the vector is pulsating) when the two-phase dip is applied. The non-circular rotation of the vector is clearly visible in the measured magnitude $u_{\mathrm{g}} = |\boldsymbol{u}_{\mathrm{g}}^{\mathrm{s}}|$ and angle $\vartheta_{\mathrm{g}} = \angle \boldsymbol{u}_{\mathrm{g}}^{\mathrm{s}}$ in Fig. 13.

Figs. 11 and 12 show the simulated waveforms of the reference observer. The corresponding waveforms of the proposed observer are shown in Figs. 6 and 7. The both observers under comparison can track the angle and magnitude of the positive-sequence voltage without steady-state errors. However, the reference observer cannot estimate the negative-sequence voltage components as the estimation error response of $\tilde{\boldsymbol{u}}_{\mathrm{g}-}$ in Fig. 12 shows. Furthermore, with the reference observer, the estimation error of the positive-sequence angle $\tilde{\vartheta}_{\mathrm{g}+}$ oscillates after transients but has lower peak values. In general, the reference observer has a simpler structure and is recommended if only the positive-sequence quantities are of interest. The proposed observer is a bit more complex but it enables the estimation of the negative-sequence voltage (in addition to the features of the reference observer).

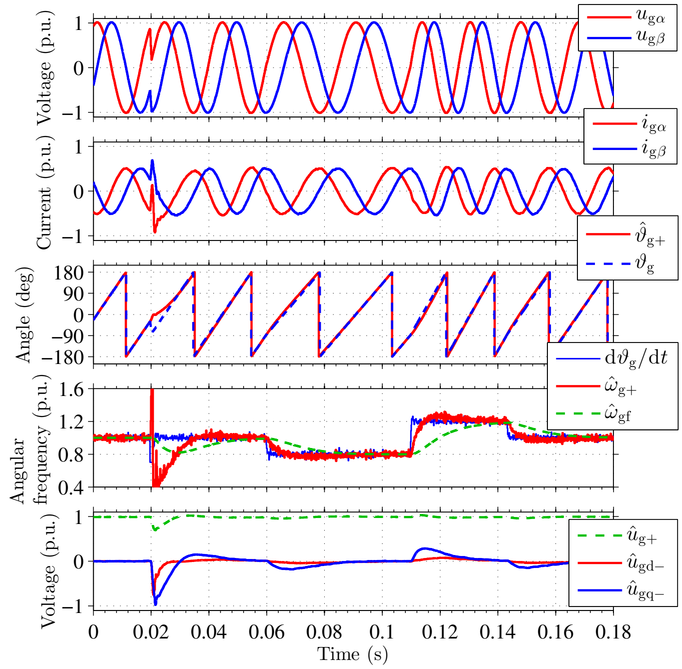

Fig. 15. Measured waveforms during the phase-angle jump of $-60°$ and frequency changes: (first) space-vector components of the grid-voltage; (second) space-vector components of the grid current; (third) estimated positive-sequence angle (solid) and actual angle of the grid-voltage vector (dashed); (fourth) estimated angular frequencies $\hat{\omega}_{\mathrm{g}+}$ and $\hat{\omega}_{\mathrm{gf}}$, and the actual angular frequency of the grid-voltage vector; and (fifth) estimated positive-sequence magnitude (dashed) and negative-sequence components (solid).

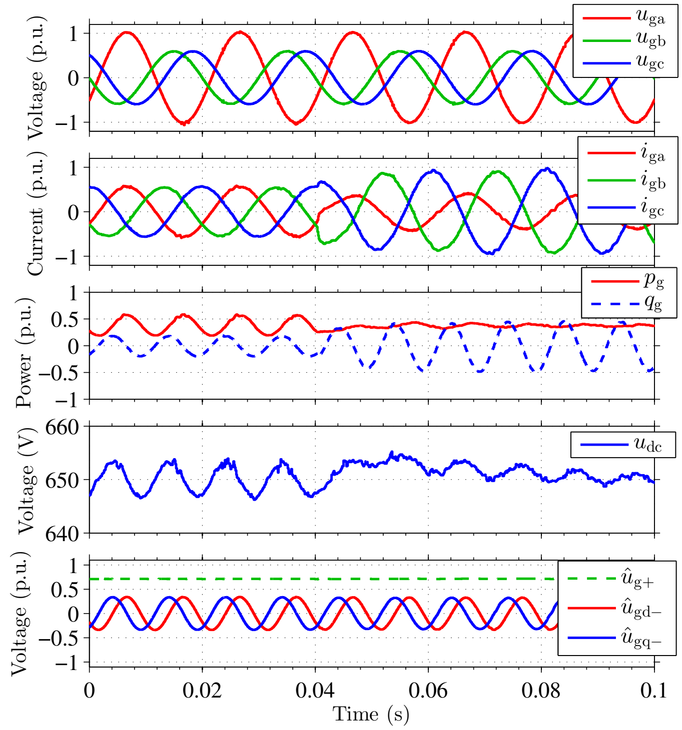

Fig. 16. Measured waveforms: (first) grid voltages; (second) grid currents; (third) active power (solid) and reactive power (dashed); (fourth) DC-link voltage; and (fifth) estimated positive-sequence magnitude (dashed) and negative-sequence components (solid). After $t = 0.04$ s, the power-ripple eliminating negative-sequence component is added into the converter-current reference.

VI. Experimental Results

The proposed adaptive observer was experimentally tested as a part of the grid-voltage sensorless control scheme shown in Fig. 1(b). The switching frequency of the 12.5-kVA, 400-V converter under test is 4 kHz. The current controller is a state-space controller [25], which is tuned to give an approximate closed-loop bandwidth of 500 Hz. The controller is augmented with a reduced-order generalized integrator at $-2\omega_{\mathrm{g}+}$ for regulating the negative-sequence current component. The estimated and filtered positive and negative-sequence grid-voltage components are used in the current reference calculation. A band-stop filter at $2\omega_{\mathrm{g}+}$ removes the second-harmonic ripple from the measured DC-link voltage in the voltage control. The system parameters are given in Table I. The pole placement of the observer follows the example analyzed in Section IV-A and simulated in Section V. The tuning parameters are given in Table II.

A. Unbalanced Grid-Voltage Dips

Figs. 13 and 14 show the measured waveforms when the following grid-voltage sequence was generated using a 50-kVA four-quadrant power supply (Regatron TopCon TC.ACS): 1) symmetrical grid conditions; 2) single-phase voltage dip down to zero; 3) two-phase voltage dip down to zero; 4) symmetrical grid conditions. During the test sequence, the converter was loaded by another back-to-back connected converter such that the converter under test was supplying the power of 0.3 p.u. Fig. 13 shows the measured magnitude $u_{\mathrm{g}} = |\boldsymbol{u}_{\mathrm{g}}^{\mathrm{s}}|$ and angle $\vartheta_{\mathrm{g}} = \angle\boldsymbol{u}_{\mathrm{g}}^{\mathrm{s}}$ (blue dashed lines) of the grid-voltage vector (1). The locus of the measured voltage vector is plotted in Fig. 14. Theoretically, the positive-sequence magnitude in the voltage vector is $2/3$ p.u. and $1/3$ p.u. during the single-phase and two-phase dips, respectively. The negative-sequence magnitudes are $1/3$ p.u. during the both dips. As Fig. 13 shows, the positive-sequence magnitude estimate converges quickly and the steady-state estimate agrees with the theoretical values. The positive-sequence angle is correctly detected as well, and it is only slightly perturbed in transients. The negative-sequence estimate also converges quickly and agrees with the theory. Moreover, the experimentally measured results match well with the corresponding simulated results, cf. Fig. 6.

As Fig. 13 shows, the grid currents are balanced even under highly unbalanced grid voltages. In the beginning, the magnitudes of the grid currents are 0.3 p.u. because the power of 0.3 p.u. is transferred. During the grid-voltage dips, the magnitudes of the currents increase first to 0.5 p.u. and then to 1 p.u. in order to transfer the same power and to maintain the power balance in steady state. The voltage transients shown in the figure are challenging but the sensorless control system is operating very well and it is able to achieve steady state approximately within a grid-voltage cycle.

B. Phase-Angle Jump and Frequency Steps

Fig. 15 shows the measured and estimated waveforms when the phase-angle jump of $-60°$ was applied at $t = 0.02$ s and the grid-voltage frequency was stepwise changed from 50 Hz to 40 Hz at $t = 0.06$ s, 40 Hz to 60 Hz at $t = 0.11$ s, and then back to 50 Hz. The converter was rectifying the power of -0.5 p.u. (drawn by the another back-to-back connected converter) during the test sequence. As the figure shows, the estimated positive-sequence angle $\hat{\vartheta}_{\mathrm{g}+}$ converges quickly after the phase-angle jump. During the angle jump, the change $(\mathrm{d}\vartheta_{\mathrm{g}}/\mathrm{d}t)$ causes an impulse in the estimated frequency $\hat{\omega}_{\mathrm{g}+}$. Then, $\hat{\omega}_{\mathrm{g}+}$ drives the estimate $\hat{\vartheta}_{\mathrm{g}+}$ to the correct value. However, the naturally filtered frequency estimate $\hat{\omega}_{\mathrm{gf}}$ (green dashed line) given by (20) is free of impulses. During the frequency steps, the estimate $\hat{\omega}_{\mathrm{g}+}$ converges rapidly whereas the estimate $\hat{\omega}_{\mathrm{gf}}$ converges slower but it is noise-free. Some cross-coupling is present between the estimated quantities, but the steady state is achieved approximately in 30 ms. In any case, the proposed observer and control system adapt to the frequency, which is shown by the grid-current components $i_{\mathrm{g}\alpha}$ and $i_{\mathrm{g}\beta}$. The frequency of the current components follows that of the voltage components $u_{\mathrm{g}\alpha}$ and $u_{\mathrm{g}\beta}$.

C. Feeding Negative-Sequence Current

The estimated negative-sequence component $\hat{\boldsymbol{u}}_{\mathrm{g}-}$ can be used in the current reference calculation, for example, in order to eliminate $2\omega_{\mathrm{g}+}$ ripple from the active power p_{g} or reactive power q_{g}. Fig. 16 shows the measured voltages, currents, and powers when a negative-sequence current component is added in the reference current at $t = 0.04$ s. The converter was supplying the power of 0.4 p.u., when the grid voltages were unbalanced ($u_{\mathrm{g}+} = 0.7$ p.u. and $u_{\mathrm{g}-} = 0.3$ p.u.). The reference for the negative-sequence current component was selected to eliminate the active-power ripple and the reference was calculated using the estimated and filtered negative-sequence voltage component. As the figure shows, the ripple is reduced in the active power p_{g}, reducing the ripple also in the DC-link voltage u_{dc}. On the other hand, the currents become unbalanced according to the instantaneous power theory and their peak value increases close to 1 p.u.

VII. Conclusion

This paper has presented an augmented adaptive observer for grid-voltage sensorless control of a grid-connected converter equipped with an LCL filter. The proposed observer can simultaneously estimate the positive- and negative-sequence components of the grid voltage even in highly unbalanced conditions. A linearized model has been derived for tuning of the observer, and the observer has been tested with computer simulations and experimentally. The results indicate fast tracking of the estimated quantities. Grid-voltage sensorless control provides redundancy in the case of sensor faults or cost savings when the voltage sensors can be eliminated. The proposed observer could be applied, e.g., in active-front-end rectifiers of motor drives or in solar inverters. In the field of grid-voltage sensorless control, a future research topic could be design and analysis of an adaptive observer including series resistances of the passive components and inductor saturation in the system model.

Appendix A
Discrete-Time State-Space Model

The detailed expressions of the system matrix $\mathbf{\Phi}$ and input vector $\mathbf{\Gamma}_\mathrm{c}$ in (3) have been presented in [25]. When $u_{\mathrm{g}+}$, $u_{\mathrm{g}-}$, and $\omega_{\mathrm{g}+}$ are assumed to be constant during the sampling period T_s, the input matrices $\mathbf{\Gamma}_{\mathrm{g}+}$ and $\mathbf{\Gamma}_{\mathrm{g}-}$ are obtained from

$$\mathbf{\Gamma}_{\mathrm{g},m} = \left(\int_0^{T_\mathrm{s}} \mathrm{e}^{\mathbf{A}\tau} \mathrm{e}^{\mathrm{j}(m-1)\omega_{\mathrm{g}+}(T_\mathrm{s}-\tau)} \mathrm{d}\tau \right) \mathbf{B}_\mathrm{g} \tag{30}$$

where $m = 1$ for $\mathbf{\Gamma}_{\mathrm{g}+}$ and $m = -1$ for $\mathbf{\Gamma}_{\mathrm{g}-}$. The matrix $\mathbf{A}$ and the vector $\mathbf{B}_\mathrm{g}$ are from the continuous-time model of the system, given in [25]. The resulting elements of the input vector $\mathbf{\Gamma}_{\mathrm{g},m} = [\boldsymbol{b}_{\mathrm{g}1,m}, \boldsymbol{b}_{\mathrm{g}2,m}, \boldsymbol{b}_{\mathrm{g}3,m}]^\mathrm{T}$ are

$$\begin{aligned}
\boldsymbol{b}_{\mathrm{g}1,m} &= \boldsymbol{\gamma}[-m\omega_{\mathrm{g}+}\omega_\mathrm{p}\sin(\omega_\mathrm{p}T_\mathrm{s}) + \mathrm{j}m^2\omega_{\mathrm{g}+}^2\cos(\omega_\mathrm{p}T_\mathrm{s}) \\
&\quad - \mathrm{j}\omega_\mathrm{p}^2\exp(\mathrm{j}m\omega_{\mathrm{g}+}T_\mathrm{s}) - \mathrm{j}\delta_m]/[m\delta_m\omega_{\mathrm{g}+}(L_\mathrm{fc} + L_\mathrm{fg})] \\
\boldsymbol{b}_{\mathrm{g}2,m} &= \boldsymbol{\gamma}[\omega_\mathrm{p}\cos(\omega_\mathrm{p}T_\mathrm{s}) - \omega_\mathrm{p}\exp(\mathrm{j}m\omega_{\mathrm{g}+}T_\mathrm{s}) \\
&\quad + \mathrm{j}m\omega_{\mathrm{g}+}\sin(\omega_\mathrm{p}T_\mathrm{s})]/[\delta_m\omega_\mathrm{p}C_\mathrm{f}L_\mathrm{fg}] \\
\boldsymbol{b}_{\mathrm{g}3,m} &= \boldsymbol{\gamma}[m\omega_{\mathrm{g}+}\omega_\mathrm{p}L_\mathrm{fc}\sin(\omega_\mathrm{p}T_\mathrm{s}) - \mathrm{j}m^2\omega_{\mathrm{g}+}^2L_\mathrm{fc}\cos(\omega_\mathrm{p}T_\mathrm{s}) \\
&\quad + \mathrm{j}\exp(\mathrm{j}m\omega_{\mathrm{g}+}T_\mathrm{s})(\delta_mL_\mathrm{fg} + m^2\omega_{\mathrm{g}+}^2L_\mathrm{fc}) - \mathrm{j}\delta_mL_\mathrm{fg}] \\
&\quad /[m\delta_m\omega_{\mathrm{g}+}L_\mathrm{fg}(L_\mathrm{fc} + L_\mathrm{fg})]
\end{aligned}$$

where ω_p is the resonance frequency of the LCL filter, $\boldsymbol{\gamma} = \exp(-\mathrm{j}\omega_{\mathrm{g}+}T_\mathrm{s})$, and $\delta_m = m^2\omega_{\mathrm{g}+}^2 - \omega_\mathrm{p}^2$.

Appendix B
Small-Signal Linearization of the Estimation-Error Dynamics

The estimation-error dynamics (12) are described by the nonlinear function

$$\begin{aligned}
\tilde{\mathbf{x}}_\mathrm{a}(k+1) = &\boldsymbol{f}[\tilde{\mathbf{x}}_\mathrm{a}(k), \mathbf{x}_\mathrm{a}(k), \boldsymbol{u}_\mathrm{c}(k), u_{\mathrm{g}+}(k), \\
&\tilde{u}_{\mathrm{g}+}(k), \tilde{\vartheta}_{\mathrm{g}+}(k), \tilde{\omega}_{\mathrm{g}+}(k)]
\end{aligned} \tag{31}$$

Equilibrium-point quantities of this system are marked with the subscript 0. If the parameters inside the observer matrices $\hat{\mathbf{\Phi}}_\mathrm{a}$, $\hat{\mathbf{\Gamma}}_\mathrm{ca}$, and $\hat{\mathbf{\Gamma}}_\mathrm{ga}$ are correct ($\hat{L}_\mathrm{fc} = L_\mathrm{fc}$, $\hat{C}_\mathrm{f} = C_\mathrm{f}$, and $\hat{L}_\mathrm{fg} = L_\mathrm{fg}$) and the frequency estimation error is zero ($\tilde{\omega}_{\mathrm{g}+,0} = \omega_{\mathrm{g}+,0} - \hat{\omega}_{\mathrm{g}0} = 0$), the system and observer matrices are equal $\mathbf{\Phi}_\mathrm{a0} = \hat{\mathbf{\Phi}}_\mathrm{a0}$, $\mathbf{\Gamma}_\mathrm{ca0} = \hat{\mathbf{\Gamma}}_\mathrm{ca0}$, $\mathbf{\Gamma}_\mathrm{ga0} = \hat{\mathbf{\Gamma}}_\mathrm{ga0}$. It follows that the nonlinear system has an equilibrium point $\{\tilde{\mathbf{x}}_\mathrm{a0} = \mathbf{0}, \tilde{u}_{\mathrm{g}+,0} = 0, \tilde{\omega}_{\mathrm{g}+,0} = 0, \tilde{\vartheta}_{\mathrm{g}+,0} = 0\}$. In the vicinity of the equilibrium point, the small-signal deviation is marked with δ, e.g., $\delta\tilde{\mathbf{x}}_\mathrm{a} = \tilde{\mathbf{x}}_\mathrm{a} - \tilde{\mathbf{x}}_\mathrm{a0}$. In terms of the small-signal deviations, the estimation-error dynamics around the equilibrium point are

$$\begin{aligned}
\delta\tilde{\mathbf{x}}_\mathrm{a}(k+1) = &\left(\frac{\partial \boldsymbol{f}}{\partial \tilde{\mathbf{x}}_\mathrm{a}}\right)_0 \delta\tilde{\mathbf{x}}_\mathrm{a}(k) + \left(\frac{\partial \boldsymbol{f}}{\partial \mathbf{x}}\right)_0 \delta\mathbf{x}_\mathrm{a}(k) \\
&+ \left(\frac{\partial \boldsymbol{f}}{\partial \boldsymbol{u}_\mathrm{c}}\right)_0 \delta\boldsymbol{u}_\mathrm{c}(k) + \left(\frac{\partial \boldsymbol{f}}{\partial u_{\mathrm{g}+}}\right)_0 \delta u_{\mathrm{g}+}(k) \\
&+ \left(\frac{\partial \boldsymbol{f}}{\partial \tilde{u}_{\mathrm{g}+}}\right)_0 \delta\tilde{u}_{\mathrm{g}+}(k) + \left(\frac{\partial \boldsymbol{f}}{\partial \tilde{\vartheta}_{\mathrm{g}+}}\right)_0 \delta\tilde{\vartheta}_{\mathrm{g}+}(k) \\
&+ \left(\frac{\partial \boldsymbol{f}}{\partial \tilde{\omega}_{\mathrm{g}+}}\right)_0 \delta\tilde{\omega}_{\mathrm{g}+}(k)
\end{aligned} \tag{32}$$

when constant $\omega_{\mathrm{g}+}$ is assumed, i.e., $\delta\omega_{\mathrm{g}+} = 0$. The partial derivatives are evaluated at the equilibrium point, and they are

$$\begin{aligned}
&\left(\frac{\partial \boldsymbol{f}}{\partial \tilde{\mathbf{x}}_\mathrm{a}}\right)_0 = \begin{bmatrix} \mathbf{\Phi}_0 & \mathbf{\Gamma}_{\mathrm{g}-,0} \\ \mathbf{0} & \mathrm{e}^{-2\mathrm{j}\omega_{\mathrm{g}+,0}T_\mathrm{s}} \end{bmatrix} - \mathbf{K}_\mathrm{o}\mathbf{C}_\mathrm{a} \\
&\left(\frac{\partial \boldsymbol{f}}{\partial \mathbf{x}_\mathrm{a}}\right)_0 = \left(\frac{\partial \boldsymbol{f}}{\partial \boldsymbol{u}_\mathrm{c}}\right)_0 = \left(\frac{\partial \boldsymbol{f}}{\partial u_{\mathrm{g}+}}\right)_0 = 0 \\
&\left(\frac{\partial \boldsymbol{f}}{\partial \tilde{u}_\mathrm{g}}\right)_0 = \hat{\mathbf{\Gamma}}_\mathrm{ga0}, \qquad \left(\frac{\partial \boldsymbol{f}}{\partial \tilde{\vartheta}_{\mathrm{g}+}}\right)_0 = \mathrm{j}u_{\mathrm{g}+,0}\mathbf{\Gamma}_\mathrm{ga0} \\
&\left(\frac{\partial \boldsymbol{f}}{\partial \tilde{\omega}_{\mathrm{g}+}}\right)_0 = \begin{bmatrix} \mathbf{0} & \mathrm{j}T_\mathrm{s}\mathbf{\Gamma}_{\mathrm{g}-,0} - \left(\frac{\partial\hat{\mathbf{\Gamma}}_{\mathrm{g}-}}{\partial\tilde{\omega}_{\mathrm{g}+}}\right)_0 \\ \mathbf{0} & -\mathrm{j}T_\mathrm{s}\mathrm{e}^{-2\mathrm{j}\omega_{\mathrm{g}+,0}T_\mathrm{s}} \end{bmatrix} \mathbf{x}_\mathrm{a0} \\
&\qquad + \begin{bmatrix} \mathrm{j}T_\mathrm{s}\mathbf{\Gamma}_{\mathrm{g}+,0} - \left(\frac{\mathrm{d}\hat{\mathbf{\Gamma}}_{\mathrm{g}+}}{\partial\tilde{\omega}_{\mathrm{g}+}}\right)_0 \\ 0 \end{bmatrix} u_{\mathrm{g}+,0} = \mathbf{\Gamma}_\omega
\end{aligned} \tag{33}$$

It is to be noted that the elements of the linearized input vector $\mathbf{\Gamma}_\omega$ are generally time-variant. The time dependence originates from the rotating negative-sequence component ($\boldsymbol{u}_{\mathrm{g}-,0} = [0,0,0,1]\mathbf{x}_\mathrm{a0}$) in $\mathbf{x}_\mathrm{a0}$. In order to shorten notation, the symbol δ denoting the small-signal deviations is dropped out in the linearized dynamics in Section III.

References

[1] T. Noguchi, H. Tomiki, S. Kondo, and I. Takahashi, "Direct power control of PWM converter without power-source voltage sensors," *IEEE Trans. Ind. Appl.*, vol. 34, no. 3, pp. 473–479, May/Jun. 1998.

[2] M. Malinowski, M. P. Kazmierkowski, S. Hansen, F. Blaabjerg, and G. D. Marques, "Virtual-flux-based direct power control of three-phase PWM rectifiers," *IEEE Trans. Ind. Appl.*, vol. 37, no. 4, pp. 1019–1027, Jul./Aug. 2001.

[3] D.-C. Lee and D.-S. Lim, "AC voltage and current sensorless control of three-phase PWM rectifiers," *IEEE Trans. Power Electron.*, vol. 17, no. 6, pp. 883–890, Nov. 2002.

[4] H.-S. Song, I.-W. Joo, and K. Nam, "Source voltage sensorless estimation scheme for PWM rectifiers under unbalanced conditions," *IEEE Trans. Ind. Electron.*, vol. 50, no. 6, pp. 1238–1245, Dec. 2003.

[5] R. Pöllänen, A. Tarkiainen, M. Niemelä, and J. Pyrhönen, "Supply voltage sensorless reactive power control of DTC modulation based line converter with L- and LCL-filters," in *Proc. EPE 2003*, Toulouse, France, Sep. 2003, pp. 1–10.

[6] M. Malinowski, G. Marques, M. Cichowlas, and M. P. Kazmierkowski, "New direct power control of three-phase PWM boost rectifiers under distorted and imbalanced line voltage conditions," in *Proc. IEEE ISIE 2003*, vol. 1, Rio de Janeiro, Brazil, Jun. 2003, pp. 438–443.

[7] I. Agirman and V. Blasko, "A novel control method of a VSC without AC line voltage sensors," *IEEE Trans. Ind. Appl.*, vol. 39, no. 2, pp. 519–524, Mar./Apr. 2003.

[8] K. H. Ahmed, A. M. Massoud, S. J. Finney, and B. W. Williams, "Sensorless current control of three-phase inverter-based distributed generation," *IEEE Trans. Power Del.*, vol. 24, no. 2, pp. 919–929, Apr. 2009.

[9] Y. A.-R. I. Mohamed and E. F. El-Saadany, "A robust natural-frame-based interfacing scheme for grid-connected distributed generation inverters," *IEEE Trans. Energy Convers.*, vol. 26, no. 3, pp. 728–736, Sep. 2011.

[10] M. Malinowski and S. Bernet, "A simple voltage sensorless active damping scheme for three-phase PWM converters with an LCL filter," *IEEE Trans. Ind. Electron.*, vol. 55, no. 4, pp. 1876–1880, Apr. 2008.

[11] M. Liserre, A. Pigazo, A. Dell'Aquila, and V. M. Moreno, "An anti-islanding method for single-phase inverters based on a grid voltage sensorless control," *IEEE Trans. Ind. Appl.*, vol. 53, no. 5, pp. 1418–1426, Oct. 2006.

[12] J. A. Suul, A. Luna, P. Rodríguez, and T. Undeland, "Virtual-flux-based voltage-sensor-less power control for unbalanced grid conditions," *IEEE Trans. Power Electron.*, vol. 27, no. 9, pp. 4071–4087, Sep. 2012.

[13] K. H. Ahmed, A. M. Massoud, S. J. Finney, and B. W. Williams, "A synchronous DQ frame controller via an LCL coupled filter under unbalanced three-phase voltage supply conditions," in *Proc. POWERENG 2011*, Málaga, Spain, May 2011, pp. 1–6.

[14] L. A. Serpa, S. Ponnaluri, P. M. Barbosa, and J. W. Kolar, "A modified direct power control strategy allowing the connection of three-phase inverters to the grid through LCL filters," *IEEE Trans. Ind. Appl.*, vol. 43, no. 5, pp. 1388–1400, Sep./Oct. 2007.
[15] G. Wrona and K. Malon, "Sensorless operation of an active front end converter with LCL filter," in *Proc. ISIE 2014*, Istanbul, Turkey, Jun. 2014, pp. 2697–2702.
[16] W. Gullvik, L. Norum, and R. Nilsen, "Active damping of resonance oscillations in LCL-filters based on virtual flux and virtual resistor," in *Proc. EPE 2007*, Aalborg, Denmark, Sep. 2007, pp. 1–10.
[17] S. Mariéthoz and M. Morari, "Explicit model-predictive control of a PWM inverter with an LCL filter," *IEEE Trans. Ind. Electron.*, vol. 56, no. 2, pp. 389–399, Feb. 2009.
[18] B. Bolsens, K. De Brabandere, J. Van den Keybus, J. Driesen, and R. Belmans, "Model-based generation of low distortion currents in grid-coupled PWM-inverters using an LCL output filter," *IEEE Trans. Power Electron.*, vol. 21, no. 4, pp. 1032–1040, Jul. 2006.
[19] J. Kukkola and M. Hinkkanen, "State observer for grid-voltage sensorless control of a converter equipped with an LCL filter: Direct discrete-time design," *IEEE Trans. Ind. Appl.*, vol. 52, no. 4, pp. 3133–3145, Jul./Aug. 2016.
[20] V. Miskovic, V. Blasko, T. Jahns, R. Lorenz, and H. Zhang, "Robust sensorless control of grid connected converters with LCL line filters using frequency adaptive observers as AC voltage estimators," in *Proc. IEEE APEC*, Long Beach, CA, Mar. 2016, pp. 2167–2174.
[21] G. Lammert, T. Hess, M. Schmidt, P. Schegner, and M. Braun, "Dynamic grid support in low voltage grids – fault ride-through and reactive power/voltage support during grid disturbances," in *Proc. Power Syst. Comput. Conf. (PSCC'14)*, Wroclaw, Poland, Aug. 2014.
[22] Y. Suh, Y. Go, and D. Rho, "A comparative study on control algorithm for active front-end rectifier of large motor drives under unbalanced input," *IEEE Trans. Ind. Appl.*, vol. 47, no. 3, pp. 1419–1431, May/Jun. 2011.
[23] P. Tourou and C. Sourkounis, "Review of control strategies for DFIG-based wind turbines under unsymmetrical grid faults," in *Proc. 9th Int. Conf. Ecol. Veh. Renew. Energies (EVER'2014)*, Monte Carlo, Monaco, Mar. 2014.
[24] J. Kukkola and M. Hinkkanen, "Grid-voltage sensorless control of a converter under unbalanced conditions: On the design of a state observer," in *Proc. IEEE ECCE 2016*, Milwaukee, WI, Sep. 2016.
[25] J. Kukkola, M. Hinkkanen, and K. Zenger, "Observer-based state-space current controller for a grid converter equipped with an LCL filter: Analytical method for direct discrete-time design," *IEEE Trans. Ind. Appl.*, vol. 51, no. 5, pp. 4079–4090, Sep./Oct. 2015.
[26] S. Skogestad and I. Postlethwaite, *Multivariable Feedback Control: Analysis and Design*. Chichester: Wiley, 1996.
[27] J.-J. E. Slotine and W. Li, *Applied Nonlinear Control*. Upper Saddle River, New Jersey: Prentice-Hall, 1991.
[28] D. Pérez-Estévez, J. Doval-Gandoy, A. G. Yepes, and O. López, "Positive- and negative-sequence current controller with direct discrete-time pole placement for grid-tied converters with LCL filter," *IEEE Trans. Power Electron.*, vol. 32, no. 9, pp. 7207–7221, Sep. 2017.
[29] R. A. Mastromauro, M. Liserre, and A. Dell'Aquila, "Study of the effects of inductor nonlinear behavior on the performance of current controllers for single-phase PV grid converters," *IEEE Trans. Ind. Electron.*, vol. 55, no. 5, pp. 2043–2052, May 2008.
[30] J. A. Suul, A. Luna, P. Rodríguez, and T. Undeland, "Voltage-sensor-less synchronization to unbalanced grids by frequency-adaptive virtual flux estimation," *IEEE Trans. Ind. Electron.*, vol. 59, no. 7, pp. 2910–2923, Jul. 2012.

Jarno Kukkola received the B.Sc.(Tech.), M.Sc.(Tech.), and D.Sc.(Tech.) degrees from Aalto University, Espoo, Finland, in 2010, 2012, and 2017, respectively.

He is currently a Design Engineer with ABB Oy Drives, Helsinki. His research interests include grid-connected converters.

Marko Hinkkanen (M'06–SM'13) received the M.Sc.(Eng.) and D.Sc.(Tech.) degrees from Helsinki University of Technology, Espoo, Finland, in 2000 and 2004, respectively.

He is an Associate Professor with the School of Electrical Engineering, Aalto University, Espoo. He has authored or co-authored more than 100 technical papers, of which more than 30 are in IEEE journals. His research interests include control systems, electric drives, and power converters.

Dr. Hinkkanen was the corecipient of the 2016 International Conference on Electrical Machines (ICEM) Brian J. Chalmers Best Paper Award and the 2016 IEEE Industry Applications Society Industrial Drives Committee Best Paper Award. He is an Editorial Board Member of IET Electric Power Applications.